

# Measurements and discrimination of drones and birds with a multi-frequency multistatic radar system

Riccardo Palamà<sup>1</sup>  | Francesco Fioranelli<sup>2</sup>  | Matthew Ritchie<sup>3</sup>  |  
Michael Inggs<sup>4</sup>  | Simon Lewis<sup>4</sup> | Hugh Griffiths<sup>3</sup> 

<sup>1</sup>Division of Geomatics, Department of Remote Sensing, Centre Tecnològic de Telecomunicacions de Catalunya (CTTC/CERCA), Barcelona, Spain

<sup>2</sup>Department of Microelectronics, Microwave Sensing Signals and Systems Group, TU Delft, The Netherlands

<sup>3</sup>Department of Electronic and Electrical Engineering, University College London, London, UK

<sup>4</sup>Department of Electrical Engineering, University of Cape Town, Rondebosch, South Africa

## Correspondence

Riccardo Palamà, Centre Tecnològic de Telecomunicacions de Catalunya (CTTC), Castelldefels, Barcelona, Spain.  
Email: [riccardo.palama@cttc.cat](mailto:riccardo.palama@cttc.cat)

## Funding information

Office of Naval Research Global (USA); Institution of Engineering and Technology; FFI (Norway); SA National Defence Force

## Abstract

This article presents the results of a series of measurements of multistatic radar signatures of small UAVs at L- and X-bands. The system employed was the multistatic multiband radar system, NeXtRAD, consisting of one monostatic transmitter-receiver and two bistatic receivers. NeXtRAD is capable of recording simultaneous bistatic and monostatic data with baselines and two-way bistatic range of the order of a few kilometres. The paper presents an empirical analysis with range-time plots and micro-Doppler signatures of UAVs and birds of opportunity recorded at several hundred metres of distance. A quantitative analysis of the overall signal-to-noise ratio is presented along with a comparison between the power of the signal scattered from the drone body and blades. A simple study with empirically obtained features and four supervised-learning classifiers for binary drone versus non-drone separation is also presented. The results are encouraging with classification accuracy consistently above 90% using very simple features and classification algorithms.

## 1 | INTRODUCTION

The increasing presence and usage of commercially available small drones is presenting commercial opportunities (e.g. applications in filming, agriculture, inspections, delivery, monitoring, and surveillance) and also challenges and potential threats (from illegal or intrusive filming to more serious smuggling of drugs into prison, disruption to airports, and potential usage of weaponised drones). Radar is one of the most promising technologies to monitor drones, as it provides operational capabilities in all weather and light conditions, with accurate estimation of range and velocities through reliable range-Doppler processing.

However, drones are challenging targets for conventional radar systems, such as those installed for air traffic control or designed to monitor larger aircraft. Drones are smaller (hence lower Radar Cross Section) and more manoeuvrable than their manned counterparts or larger Unmanned Aerial Vehicles

(UAVs), meaning that they can be removed with the clutter during the detection or lost during the tracking process. Increasing the sensitivity of the radar does help, but the related challenge is then the significant number of false targets due mostly to birds and moving non-drone objects (such as vegetation or wind turbines) that can still be in the main lobe or sidelobes of the radar [1, 2].

While the best radar systems and signal processing algorithms for optimal detection, tracking, and classification of drones are being actively investigated, it can be argued that access to multistatic/networked radar data can improve performances due to the multi-perspective views on the targets of interest and inherent resilience in cases where the target is occluded, or the data is degraded at one of its nodes. The same reasoning applies to other types of challenging targets, for example, small boats against intense sea clutter background. The majority of research available in the open literature on the radar signature of drones assumes monostatic geometries, with

limited analysis of multistatic experimental drone data performed in some of the authors' previous work [3–5]. These used the NetRAD system, the S-band pulse-Doppler radar developed in collaboration between UCL and the University of Cape Town, made of three separate but identical nodes [6]. A key capability of the NetRAD system was the possibility to collect simultaneous measurements of monostatic and multistatic signatures of targets and clutter, allowing a direct comparison to be made.

This article is an extended version of our previous contribution presented at the 2019 SEE International Radar Conference in Toulon, France [7]. That paper presented initial results of an experimental campaign involving the successor of the NetRAD system, called NeXtRAD. NeXtRAD has been developed to improve overall capabilities following the experience of using NetRAD in trials. The new radar is capable of operating in dual-band configuration (L- and X-bands, albeit not simultaneously, but alternating by pulse repetition interval, PRI), collecting polarimetric data at X-band, and operating in multistatic geometries across baselines of the order of hundreds of metres by means of GPS-Disciplined Oscillators [8–10].

While the conference paper presented only an empirical analysis of the signatures of UAVs in the range-time and micro-Doppler domains, this article expands such analysis. A quantitative analysis of the drone SNR is presented for different bands, polarisations and geometries of acquisition. Another contribution consists of the analysis of the relative level of the Doppler components due to the rotational motion of the drone blades with respect to the body zero-Doppler component. Furthermore, simple but yet effective features are presented to classify drones (observed at both X- and L-bands) versus non-drones targets (birds either flying individually or as part of a flock). The considered features are derived from sections of the micro-Doppler spectrograms, as well as from their Singular Value Decomposition (SVD) processing, mostly with the aim of exploiting the signatures of the rotor blades to identify drone targets. Good classification performances above 90% are demonstrated with simple supervised-learning classifiers such as Nearest Neighbour, Support Vector Machine, and an Ensemble classifier described in Section 3. While this simple classification study yielded good results, its limitations have to be considered, namely the amount of data restricted to those recordings with high signal-to-noise ratio where the targets signatures are well visible. Nevertheless, the demonstrated capabilities of high classification rates for targets at several hundred of metres is considered valuable in comparison with state-of-the-art systems and experiments that have been reported.

The remainder of this article is organised as follows. Section 2 presents the properties of the NeXtRAD system and describes the data collection. Section 3 illustrates the results obtained, in terms of the empirical description of Range-Time-Intensity maps and spectrograms, and feature extraction and classification for the drone versus non-drone recognition problem. Final remarks are drawn in Section 4.

## 2 | THE NeXtRAD RADAR SYSTEM AND DATA COLLECTION

As shown in Figure 1, NeXtRAD is composed of three different nodes interconnected by a wireless network and operated by a master interface from the ‘Command & Control’ (CnC) computer. The CnC node can access all the local computers at each radar node (the so-called ‘node controllers’ (NC)), but at the same time NC also allow local operators access for quality control during data collection and experiments. Each node is equipped with a GPS Disciplined Oscillator (GPSDO) [10] to establish and maintain time and phase coherency during operations, which is fundamental for collecting valuable bistatic data in the Doppler domain. Video cameras are also mounted at the antenna pedestal for each node to allow recording of the ground-truth video data, which can be extremely valuable for comparison with the radar data.

One of the nodes, Node 0, depicted at the top of Figure 1, is the designated transceiver equipped with high power amplifiers (capable of peak power of approximately 400 W at X-band and 1.6 kW at L-band), and frequency-tuneable waveform generator. The typical operating frequencies are 8.5 GHz at X-band and 1.3 GHz at L-band. The effective analogue bandwidth of the system is 45 MHz, which translates into an approximate range resolution of 3.3 m. The additional two radar nodes are used as passive, receiver-only nodes.

Each receiver can simultaneously collect both polarimetric V and H X-band channels, meaning that in X-band, full polarimetric data can be captured using alternating polarised pulses or with two consecutive measurements using different transmitted polarisation. The data are recorded in binary format as three individual channels of 16-bit in-phase and quadrature samples, with an effective sample rate of 180 MHz.

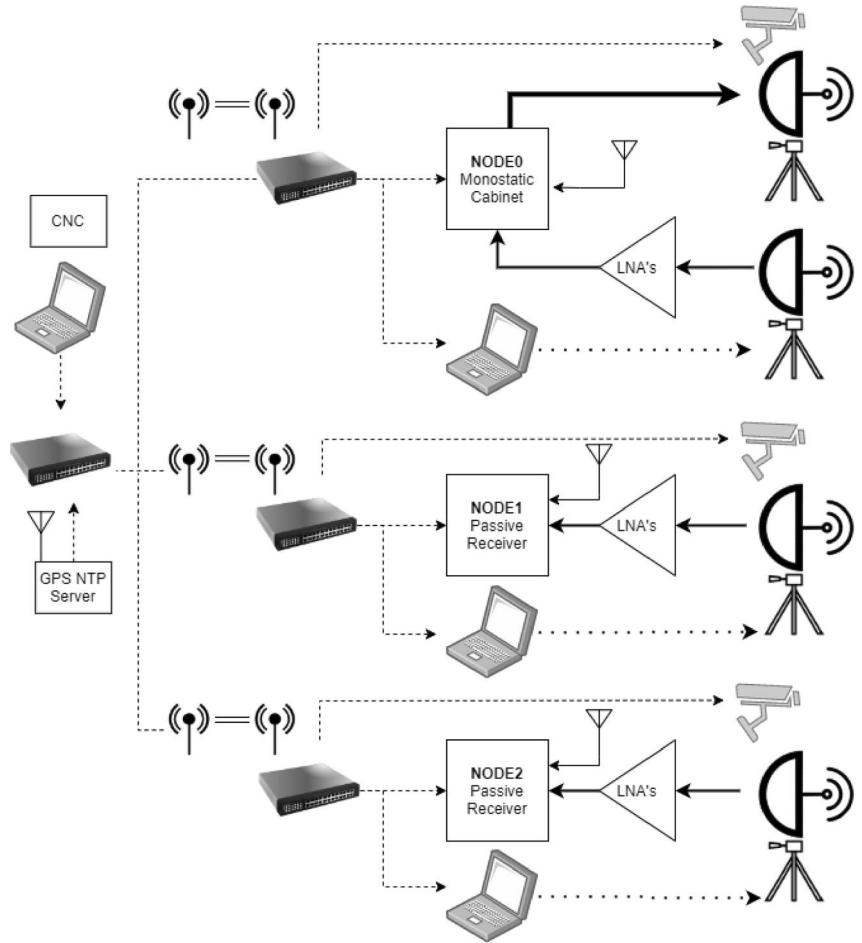
At L-band, where Doppler ambiguity requirements are less stringent, only one receiver chain is present, meaning that four measurements would be needed to collect complete polarisation data. At this stage, accounting for the very high cost of fast RF switches operating at such high transmitted power in L-band, changes in transmitted polarisation are done with slower manual switches.

The system is operated through a unified GUI interface where the operators can set specified parameters (such as carrier frequency, pulse length, Pulse Repetition Frequency PRF, number of pulses, polarisations), which are then shared over the networks using a configuration header file to all radar nodes. Included in the header file is the epoch trigger time, which is a future UTC timestamp that sets the start time of each radar recording. Data and metadata (the header file with the aforementioned parameters, as well as videos for ground-truth) are then stored as HDF5 files for further processing.

### 2.1 | Synchronisation and networking

Each node is equipped with an ovenised crystal oscillator (OCXO)-based GPSDO to establish time and frequency

**FIGURE 1** Simple schematics of the NeXtRAD system, with one active transceiver, Node 0 (top), and two passive receivers, Nodes 1 and 2. GPS and WiFi antennas are fixed to collapsible masts to improve line-of-sight. L- and X-band antennas are placed on electronically steerable pedestals. Solid arrows represent low-loss coaxial cables, whilst dotted lines and double bars represent computer cabling and wireless connections respectively



synchronisation [10], as well as geospatial WSG84 coordinates for radar geometry requirements. Relative time accuracy between the transmitter and passive nodes on the order of a few nanoseconds is required for range accuracy at the given radar bandwidth, whilst frequency accuracy and phase stability during the CPI is required for Doppler processing. The GPSDOs are operated under the common-view time and frequency transfer principle, which provides epoch trigger accuracy with an approximate RMS uncertainty of 4 ns, and relative frequency uncertainty (Overlapping Allan Deviation) of  $5e-11$  at 1 s averages. The radar has been also synchronised using a fibre-optic White Rabbit network [10], which improves the epoch trigger accuracy to below a nanosecond, reduces the relative phase drift, and removes the reliance on GPS in GPS-denied scenarios.

Experiments are initiated by distributing the header file from the CnC over a secure shell to each node using 5 GHz directional WiFi links. Upon receiving the header, each node is automatically configured to the chosen parameters, and each subcomponent is armed accordingly. When the epoch timestamp is reached, each GPSDO fires a ‘mainbang’ pulse on the averaged UTC transition, which triggers the Timing and Control Unit (TCU). The TCU is an integrated FPGA and ARM controller that is responsible for triggering the PRF, biasing the HPAs, and switching the transmitted carrier on a pulse-to-pulse basis. Additionally, each TCU can be programmed with variable delays

(with a resolution of 10 ns) to minimise static time offsets between the nodes during calibration.

## 2.2 | Trial geometry and drones

In this article, we report some preliminary results where the system was operated over relatively long baselines in the range of hundreds of metres. These were collected over a couple of weeks of experimental campaign performed in December 2018, in Simon's Town, South Africa, with the collaboration of academic partners (UCT, UCL, University of Glasgow) and FFI (Norway). Figure 2 shows a map with key locations around the area of Simon's Town within False Bay. The monostatic transceiver (yellow arrow) was located on the outdoor terrace (with antennas on the pedestal looking out towards the sea, as shown in Figure 3). The bistatic nodes were located at different positions during the trials, but the most notable ones are shown by the red arrows (the closest one at Lower North, about 2.7 km from the transceiver, and the furthest one at Else Bay, about 4 km from the transceiver). The green circle on the right-hand side represents the location of a lighthouse, Roman Rock, which is located at approximately 1.8 km from the transceiver and that was often used as static reference targets for range calibration and antenna



**FIGURE 2** Location map of the experimental campaign performed in December 2018 near Simon's Town, South Africa. The yellow arrow corresponds to the position of the monostatic transceiver; red arrows show the position of the two bistatic receivers (Lower North, LN, the closest one, and Elsie Bay, EB, the furthest one); the green circle to the right corresponds to the position of a lighthouse, Roman Rock RR, used as a reference target. The orange circle highlights approximately the area where the hexacopter was flying



**FIGURE 3** Antennas on three rotating pedestals at the location of the monostatic transceiver radar node. L-band antennas are the meshed reflectors at the top of each pedestal, where the feed is also visible; X-band antennas are cone-shaped horn antennas, located to the bottom-left of the L-band reflectors. The antennas are aligned to point to the same direction

alignment. The measurement campaign involved the collection of radar returns from a hexacopter (DJI Matrice) and a quadcopter (DJI Phantom), flying over the sea surface at a maximum distance of about 500 m from the monostatic transceiver for safety reasons. Both UAVs had rotor blades made of carbon fibre. In this article, we focus on presenting results with the hexacopter signature for its higher RCS and better visibility.

The UAVs were equipped with a GPS logger device, which collected the latitude and longitude of the object with a sampling interval of about 0.2 s. Figure 4 shows an example of the plots of the monostatic range (i.e. the distance between the target and the monostatic transceiver), of the two-way bistatic range (i.e. the sum of the monostatic range transmitter to target, plus the distance between the target and the bistatic receiver located at Lower North), and the bistatic angle. We observe that during an interval of 20 s, the target covers about

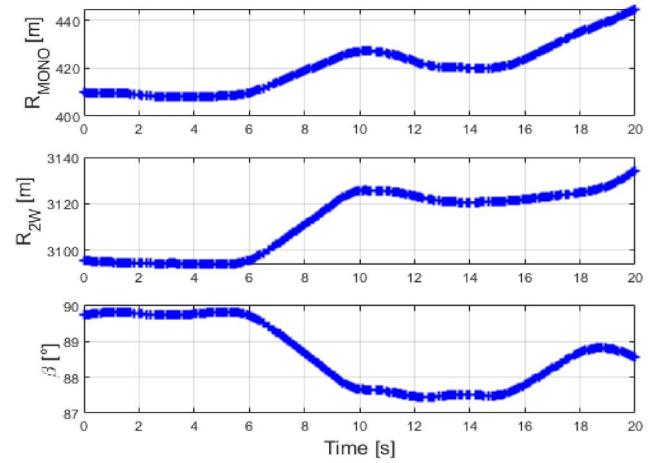


**FIGURE 4** Plots of the monostatic range, two-way bistatic range and bistatic angle as a function of time, extracted by the GPS logger mounted on the hexacopter. Dataset collected on 14 December 2018; timestamp 10.35.43

30 m along the monostatic range (from 410 to 440 m) and 40 m along the bistatic range (from 3090 to 3135 m). The values of the bistatic angle are included between  $87.5^\circ$  and  $90^\circ$ . It can be noted that the bistatic angle is inversely related to the bistatic range, since increasing (or decreasing) values of the bistatic range give decreasing (or increasing) values of the bistatic angle ( $\beta$ ). Bistatic angles in that range are very much of interest to explore the scattering mechanisms and the consequent signatures of targets.

### 3 | EXPERIMENTAL RESULTS

#### 3.1 | Empirical analysis of the results

This section presents the initial results obtained analysing the data collected in the measurement campaign performed in Simon's Town, in the first two weeks of December 2018. Figure 5 shows the normalised Range-Time-Intensity (RTI) maps of radar signatures of the hexacopter, for X-band and HH polarisation (i.e. both the transmitter and receiver antennas were horizontally polarised). The RTI maps represent the intensity of the received signal as a function of the slow time (on the vertical axis) and of the two-way range, which is calculated for both the monostatic and the bistatic data, as the sum of the transmitter-to-target plus target-to-receiver distances. These maps are normalised versus the overall maximum of the figure to have a uniform colour scale and allow qualitative comments, whereas quantitative comments are drawn from the calculation of the signal-to-noise ratio (SNR). The SNR of the hexacopter has been systematically measured by selecting from the RTI maps the range-time window where the target is located, and extracting the pulse-wise maximum, which is a rough estimate of the signal amplitude. Finally, we extract the overall maximum and the mean of the SNR time-series obtained from the previous step,

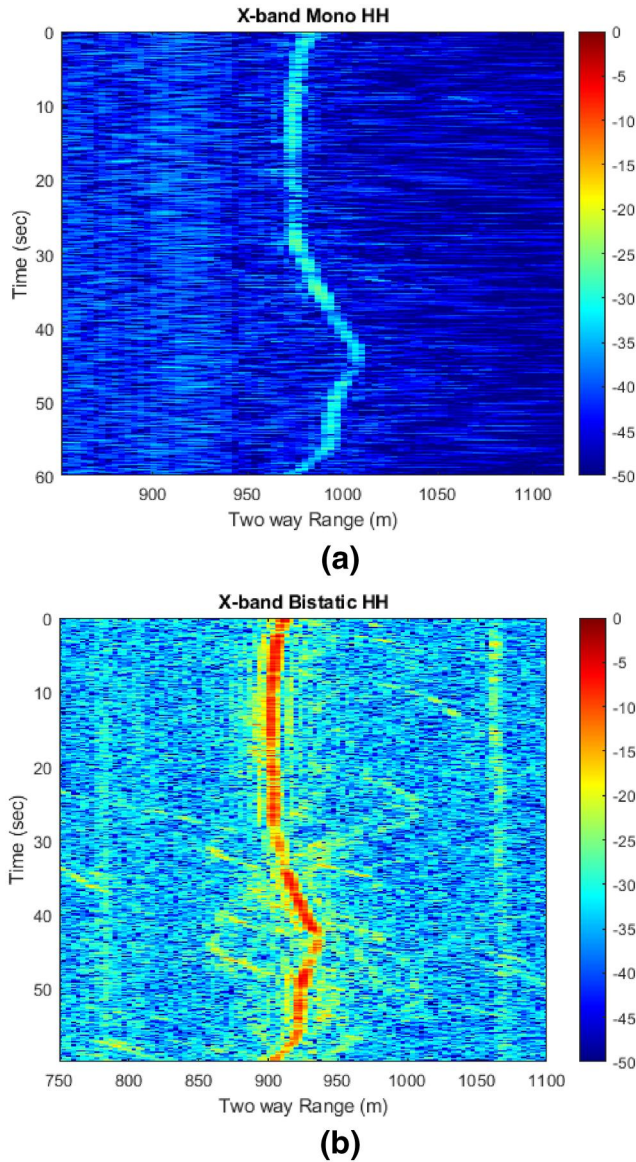


**FIGURE 5** Range-Time-Intensity maps of the monostatic (a) and short-baseline bistatic (b) X-band returns of the hexacopter at horizontal polarisation

whereas the noise level is the average amplitude of a range cell containing only noise.

The monostatic RTIs (Figure 5a) show a higher SNR with respect to the bistatic RTIs (Figure 5b). The monostatic appears weaker in Figure 5 due to high close in clutter returns meaning this range section is not noise limited compared to the bistatic node data. The bistatic RTIs show the presence of scatterers different from the UAV between 30 and 50 s. A possible source of these radar returns are the birds (mostly seagulls and cormorants) that were flying around the drone during the collection. Table 1 shows the maximum and mean values of the monostatic and simultaneous bistatic SNR for a series of datasets collected on the 13th and 14th of December 2018. The table links the values of the SNR with the band, polarisation, two-way range ( $r_{2w}$ ) of the monostatic and

bistatic node, bistatic angle ( $\beta$ ) and trajectory of the drone. It should be noted that small values of the bistatic angle ( $8^\circ$ – $9^\circ$ ) are associated with the measurements realised with short bistatic baseline (147 m), whereas large values of  $\beta$  (around  $90^\circ$ ) are obtained with large baseline (2.7 km). The values of the SNR are in general larger in L-band with respect to X-band, which is consistent with the higher transmit power employed in the L-band subsystem.

We observe that the mean monostatic SNR ranges from 35 to 45 dB in L-band, with maximum values included between 48 and 58 dB. The X-band co-polarised data show mean SNR values of 33–34 dB and maxima of 42–45 dB. The X-band cross-polarised data show large variations between the two datasets collected, where the mean values are 20 and 25 dB, and the maxima are 31 and 38 dB. The difference among the SNR values for datasets with comparable values of the drone two-way range may be due to the different drone trajectories. The drone in hovering condition covers a very small interval of aspect angles, thus a small variance of the SNR values is expected. Conversely, when the drone covers circular or random trajectories, multiple aspect angles are obtained, thus yielding higher variance of the SNR values, thus higher maxima are expected. Similar considerations can be drawn for other datasets showing different SNR values for identical bands and polarisations and comparable range intervals.

More complex is the analysis of the bistatic data, which are characterised by higher degrees of diversity, as the transmitter and receiver aspect angles are not necessarily identical and the bistatic angle is an additional factor to consider. In general, bistatic data show lower SNR values than monostatic ones, and the difference increases with larger bistatic angle. The first datasets were collected at shorter bistatic two-way ranges and with bistatic angles included roughly between  $8^\circ$  and  $10^\circ$ , yielding a quasi-monostatic geometry of acquisition. For those datasets, the gap between the monostatic and bistatic SNR values is about 13–15 dB and 10–12 dB for L- and X-band co-polarised data, respectively. This difference decreases to 5 dB for X-band cross-polarised data. The remaining datasets were collected at large bistatic angles ( $88^\circ$ – $91^\circ$ ) and larger bistatic two-way ranges ( $>3$  km). The gap between the monostatic and bistatic mean SNR values is about 11 dB and 19–27 dB for X- and L-band, respectively. For the cross-polarised X-band data, the difference is about 16 dB. It should be noted that for the datasets collected at large bistatic angle, the drone is located within a range interval where the side-lobes of the direct signal coming from the transmitter are still present, which has made more difficult the extraction of the SNR values.

The drone micro-Doppler signatures were extracted using the Short Time Fourier Transform (STFT), with a moving window of 200 temporal samples, corresponding to 200 ms, with a 50% overlap, and the number of frequency samples equal to 1024. The analysis of the micro-Doppler signature was performed on the monostatic and bistatic data collected at lower bistatic angles (upper part of Table 1). We observe that the monostatic and bistatic micro-Doppler signatures of the hexacopter at X-band (Figure 6) show a similar behaviour and that the presence of scatterers different from the UAV noticed

**TABLE 1** Measured values of the Signal-to-Noise Ratio. For legibility, the dataset recorded at the X-band have been shaded in green colour and those at L-band in yellow colour.; top four recordings collected with small bistatic angle  $\sim 9^\circ$  (quasi-monostatic configuration) and bottom five recordings collected with large bistatic angle ( $\sim 90^\circ$ )

Date/Time	Band	Pol	Mono Mean SNR (dB)	Mono Max SNR (dB)	Bi Mean SNR (dB)	Bi Max SNR (dB)	Mono $r_{2w}$ (m)	Bi $r_{2w}$ (m)	$\beta$	Trajectory
2018-12-13/16:02:38	X	HH	34	42	24	34	970–1000	1090–1120	9.2°	Hovering then linear
2018-12-13/16:02:38	X	HV	20	31	15	25	970–1000	1090–1120	9.2°	Hovering then linear
2018-12-13/16:08:26	L	HH	44	58	31	42	920–970	1040–1090	9.5°	Circles
2018-12-13/16:10:53	L	HH	45	57	30	41	940–1100	1070–1220	8.8°	Circles-random
2018-12-14/10:33:05	X	HH	33	45	14	19	950–1080	3160–3210	89°	Random
2018-12-14/10:33:05	X	HV	25	38	9	19	950–1080	3160–3210	89°	Random
2018-12-14/10:35:56	L	HH	41	54	27	39	840–960	3100–3160	89°	Random
2018-12-14/10:41:17	L	HH	41	55	14	24	830–900	3080–3120	90°	Random
2018-12-14/10:44:12	L	HH	35	48	14	21	1137–1257	3222–3263	88°	Small circles

in the RTI maps between 30 and 50 s is confirmed by the spectrograms in Figure 6.

In Figure 7, we compare the monostatic and bistatic micro-Doppler signatures of the hexacopter at L-band and HH polarisation. During the selected time interval, the drone was hovering for the majority of the time, thus its bulk yields a strong stationary component at zero Doppler. We note the presence of strong micro-Doppler returns extended within the whole spectral interval, that is between  $-500$  and  $500$  Hz. These micro-Doppler signatures are not time-stationary, as their intensity changes with time, which is probably due to small variations of the pitch and roll angles of the drone. For instance, we observe an increase of the intensity between 40 and 45 s, for both monostatic and bistatic data. We observe that the micro-Doppler signatures of the monostatic and bistatic data shown in Figure 6 are quite similar, which is probably due to the fact that the data are plotted from measurements at lower bistatic angles ( $\sim 9^\circ$ ).

The micro-Doppler signatures of the drone highlight the presence of different components, which can be roughly divided in two groups, that is the scattering from the body, which is stationary, thus centred at zero Doppler in the case that the drone is hovering, and the component due to the rotational motion of the drone blades, which is often referred to as Helicopter Rotor Modulation (HERM) lines [2]. Such component appears as minor peaks in the short-time Doppler spectrum whose amplitude and spacing depends on radar parameters, such as PRF and band, as well as on the rotational speed of the blades.

For values of the PRF greater or equal to the rotational frequency ( $f_p$ ) of the blades, the scattering from the blades would appear as a sinusoidal component in the Doppler spectrum, whereas if the PRF is lower than  $f_p$ , the radar samples the blade sinusoidal component at particular Doppler values, yielding the HERM lines. Aliasing occurs for low transmit frequencies, yielding overlapping non-zero Doppler components such as those revealed by the L-band spectrograms in Figure 7.

In order to study the level of the body and blade Doppler components, the plots in Figure 8 (monostatic) and Figure 9 (bistatic) show the signal power as a function of the Doppler frequency. These plots were obtained by averaging the spectrogram values over a window of 20 ms, and the datasets considered cover the case of hovering drone with small bistatic angle. In the plots we highlight the higher minor peaks in the Doppler spectra, that is the higher HERM line. We observe that the relative level of the blade Doppler component is the lowest in the X-band HH data, equal to about  $-10$  and  $-11$  dB for the monostatic and bistatic nodes, respectively. For the X-band monostatic HV data, the first HERM line is about 3.7 dB lower than the body zero-Doppler line, whereas this gap is reduced to 8.4 dB for bistatic data. In general, X-band data show that the relative level of the HERM lines is higher for bistatic data with respect to the monostatic ones. This behaviour is more evident in the cross-polarised data, where the bistatic HERM lines are almost at the noise level, as shown in Figures 8b and 9b. On the other hand, L-band data show an opposite behaviour with respect to X-band: Figures 8c and 9c show that the highest blade-to-body ratio is about 7 and 4 dB for the monostatic and bistatic data, respectively.

By observing the plots in Figures 8 and 9, the values of the Doppler frequencies of the highest HERM line can also be evaluated. These values are in general higher in L-band (78 and  $-90$  Hz) with respect to X-band (83 Hz for monostatic HH, 66 Hz for bistatic HH, 64 Hz for monostatic HV). As a general comment, the values the higher HERM Doppler frequency are similar between monostatic and bistatic data, which can be justified by the fact that the datasets have small bistatic angle.

### 3.2 | Feature extraction and classification results

The data presented empirically in the previous sections were analysed and the best files selected based on the SNR and

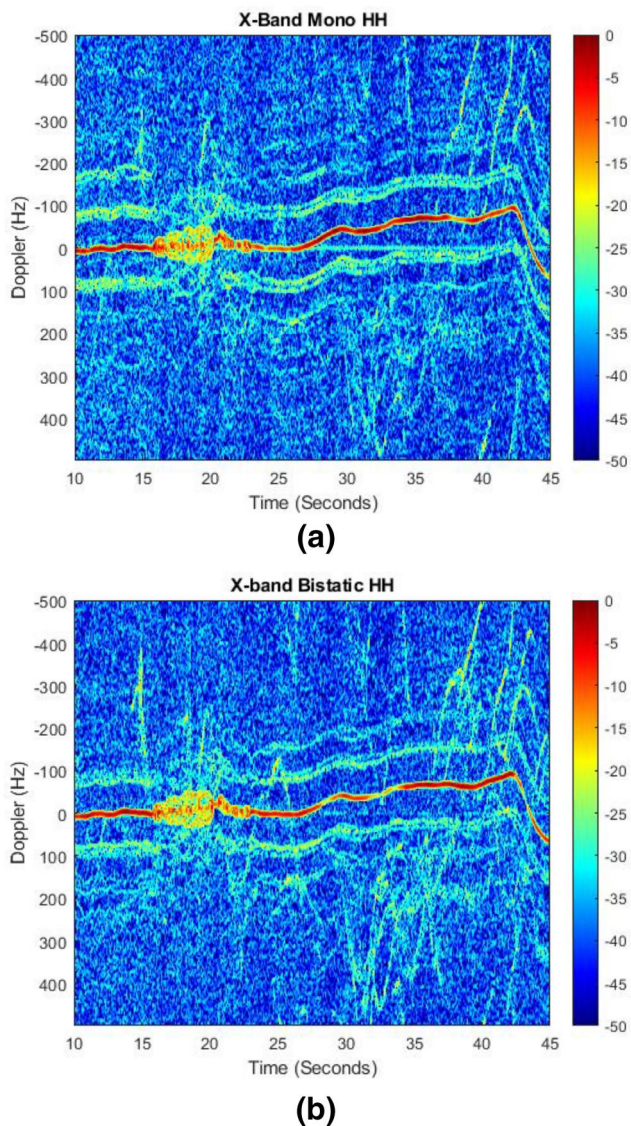


**FIGURE 6** Normalised spectrograms of X-band monostatic (a) and short-baseline bistatic (b) signatures of the hexacopter at horizontal polarisation

clarity of view of the available targets, specifically drone versus non-drone targets. Non-drone data were files with the signatures of single birds or flocks of multiple birds.

The discrimination of drones versus non-drone targets, specifically large sea birds, has been investigated in the literature in the past few years [2, 11–14], but it is still an outstanding research challenge. In total, 231 s of data were selected for usage in the classification analysis, namely 100 s of drone data at L-band, 71 s of non-drone data at L-band, and 60 s of drone data at X-band.

Unfortunately, the SNR of the bird targets at X-band was not sufficient to comprehensively analyse these targets. This limits the possibility to perform a balanced comparison of drone versus non-drone targets in the two bands separately. All in all, the data for the classification analysis shown in this paper

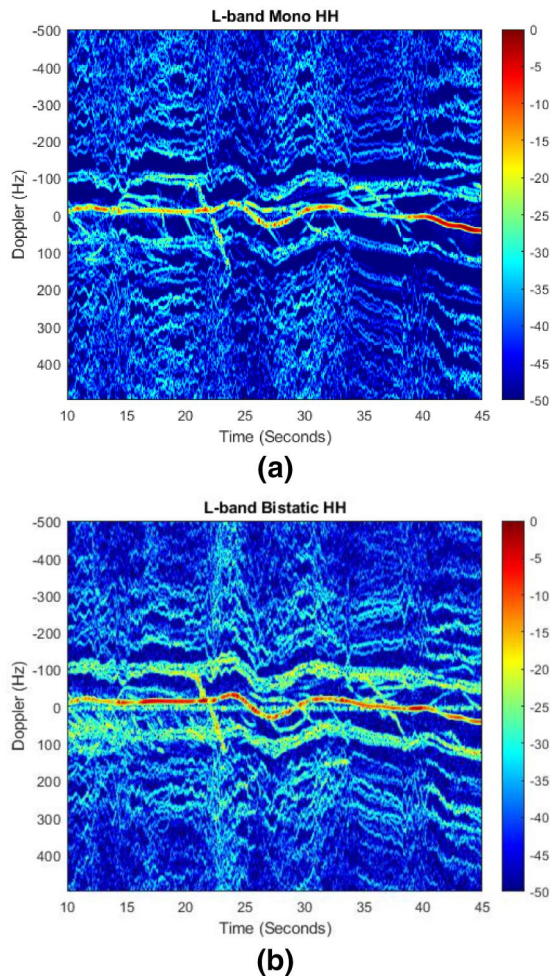


**FIGURE 7** Normalised spectrograms of L-band monostatic (a) and bistatic (b) radar signatures from the hexacopter. Data collected on 14 December 2018, bistatic baseline of 2.7 km, bistatic angle of about  $90^\circ$

were monostatic HH co-polarised data, selected for the clearer signature of the rotor blades.

These data were analysed so as to isolate the parts of range-time matrices containing target signatures. Their micro-Doppler spectrograms were then calculated and divided into 1 s long segments. These segments were then used to extract feature samples, in total 10 different features from each sample. Figure 10 shows for completeness three L-band spectrograms of the drone (Figure 10a) and non-drone objects, namely a single (or a very limited number of birds) in Figure 10b, and many birds flying together in a flock in Figure 10c.

The obvious difference, visible empirically by eye, is the presence of rotor blades contributions in the drone signatures. The information contained in these rotor blades' modulations is very rich and, besides the problem of discrimination of drones versus non-drones, has been exploited successfully also to differentiate between different models of drones [15, 16].

The ten features considered in this work were:

- Maximum value, mean value, variance, and sum of all the pixels values in the positive (Doppler values  $> 0$ ) region of

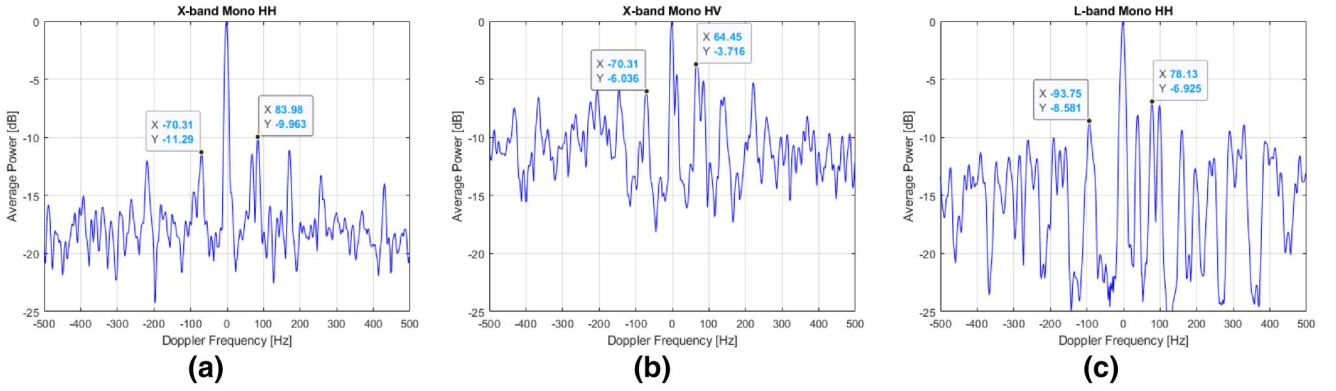


**FIGURE 8** Plots of the normalised power as a function of the Doppler frequency, obtained by averaging the spectrograms over a window of 20 ms, in the case of hovering drone. Monostatic node. X-band HH (a) and HV (b), L-band HH (c)

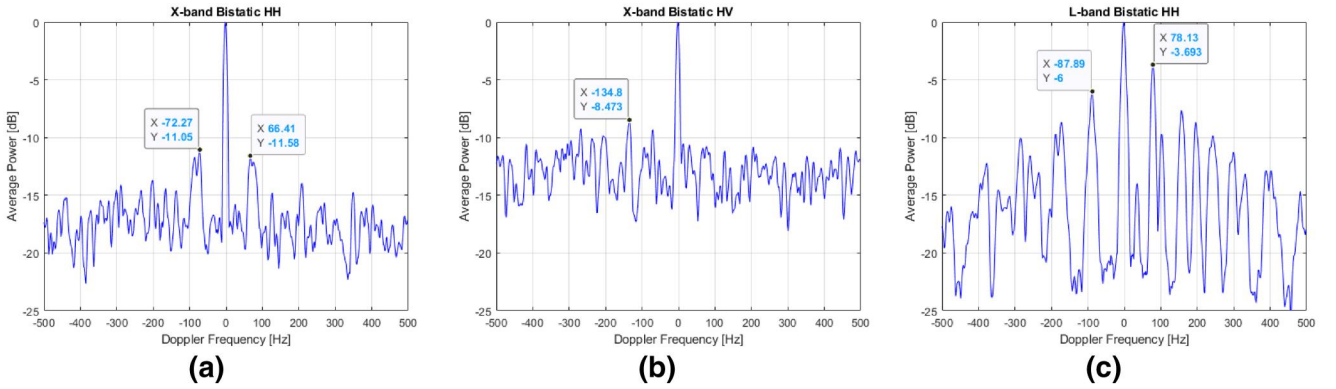


**FIGURE 9** Plots of the normalised power as a function of the Doppler frequency, obtained by averaging the spectrograms over a window of 20 ms, in the case of hovering drone. Bistatic node. X-band HH (a) and HV (b), L-band HH (c)

the micro-Doppler spectrum, calculated as the upper 37.5% of the Doppler bins from the 0 Hz;

- Maximum value, mean value, variance, and sum of all the pixels values in the negative (Doppler values < 0) region of the micro-Doppler spectrum, calculated as the lower 37.5% of the Doppler bins from the 0 Hz;
- Mean and variance of the singular values in the matrix  $\mathcal{S}$ , resulting from the SVD (Singular Value Decomposition) of the 1s spectrogram segment  $\mathbf{N}$ , whereby  $\mathbf{N} = \mathbf{U}\mathbf{S}\mathbf{V}^T$ .

The features were empirically selected (or ‘handcrafted’ as described by some authors), meaning that the process to calculate them and extract their values required significant manipulations of thresholds and parameters. This contrasts with other, more recent data-driven approaches where the relevant features can be extracted directly by the classification algorithm, typically a neural network, limiting or completely eliminating the need of pre-processing steps performed by the human operator who analyses the data.

The 10 features extracted are selected using a so-called filter method [17] based on the  $T$ -test. The features are ranked in terms of their quality based on the clustering of their samples in terms of inter-class and intra-class differences, whereby good features (highly ranked) are those maximising

the former difference and minimising the latter. Four features out of the initial pool of 10 were selected and denoted by A–D. These were (A) the maximum value of the negative Doppler region, (B) the mean of the singular values of the SVD, (C) the variance of the singular values of the SVD, and (D) the variance of the positive Doppler region. All possible combinations (15) of these four selected features were tested, starting with single feature classification (A; B; C; D), pairs of features, triplets of features, and all four features together.

Four classifiers were used, namely Naïve Bayes (NB), Nearest Neighbours with three neighbours (KNN), Support Vector Machine (SVM) with quadratic kernel, and an ensemble classifier based on ‘bags of trees’ (ET) [18]. The classifiers are trained with 50% of the available feature samples and tested with the remaining 50%. The process is repeated 50 times with random selection of training and testing samples and the final results averaged, to reduce overfitting given the small size of the available dataset.

Results are presented in the remainder of this section. Figure 11 shows the classification accuracy for the four classifiers as a function of the combinations of selected four features. It should be noted that the classification problem here was binary drone versus non-drone, where samples for the drone classes included both X- and L-band data. The

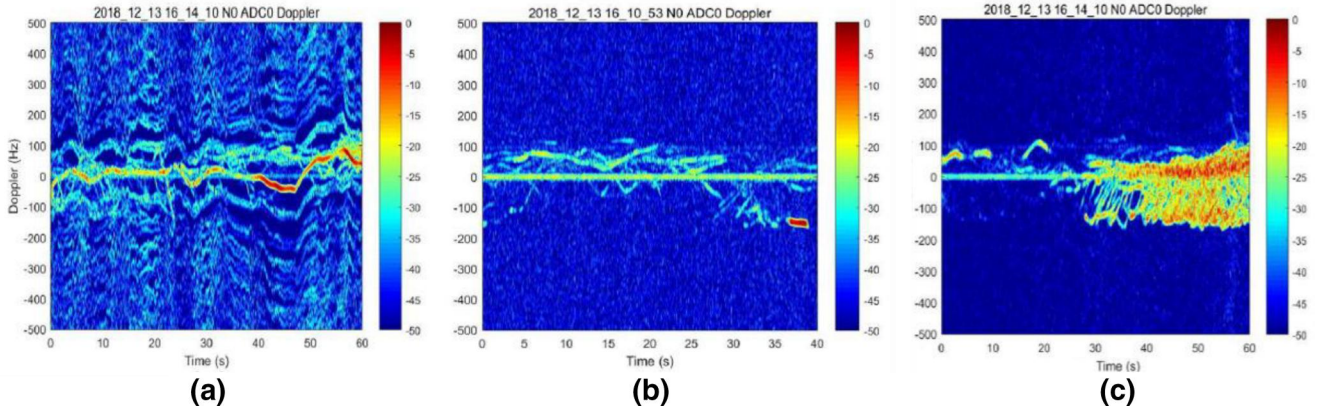


**FIGURE 10** Normalised spectrograms of L-band monostatic signatures of the drone (a), single or limited number of birds (b), and many birds in a large flock (c)

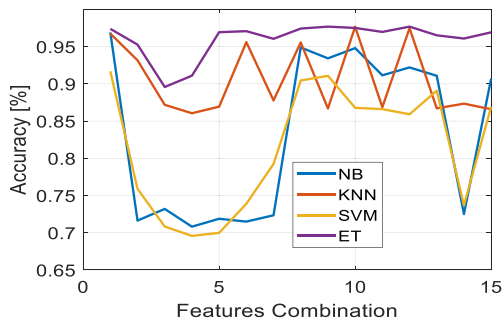


**FIGURE 11** Classification accuracy as a function of combinations of the four selected features for different classifiers. Binary classification drone (L + X-band) versus non-drone data (L-band)

ensemble classifier appears to outperform the other classifiers, both in terms of the achieved values of accuracy and in terms of its performance stability being less affected by the selection of the features. This is not surprising as the idea behind an ensemble classifier is to combine the results from a group of multiple weak classifiers to yield better results through this combination [18].

Table 2 shows the maximum, minimum, mean, and standard deviation values across the 50 cross-validation tests for the considered best case, that is the case achieving the highest accuracy on average across all possible feature combinations. The maximum/minimum values and the standard deviation are reported to show the distribution of the results around the mean value, in particular looking at the worst case (the minimum value) to ensure that it does not degrade below an acceptable threshold. In this case, the ensemble classifier provides approximately 95% minimum accuracy value, which is an encouraging result.

Table 3 shows the corresponding confusion matrix (case of the ensemble classifier, with the feature combination yielding the highest mean accuracy). This enables to see where misclassification events happen, and in case there are more missed detection of real drones or false alarms due to non-drone samples classified as drones. It should be noted that

**TABLE 2** Maximum, minimum, mean, and standard deviation values for the best (on average) result across the feature combinations

	MAX	MIN	MEAN	STD
<b>NB</b>	0.98	0.94	0.97	0.01
<b>KNN</b>	1.00	0.94	0.98	0.01
<b>SVM</b>	0.97	0.83	0.92	0.03
<b>ET</b>	1.00	0.95	0.98	0.01

**TABLE 3** Confusion matrix across the 50 cross-validation attempts for the best feature combination – ET classifier

	Predicted non-drone	Predicted drone
<b>True Non-drone</b>	1669	81
<b>True drone</b>	52	3948

the classifiers were trained in this case assuming a 50% probability across the two classes and with the same penalty cost for misclassification for both missed detection and false alarms. Note also that the matrix shows the values in terms of samples across the 50 cross-validation tests (80 drone samples and 35 non-drone samples for each test, for 50 tests in total, yielding to 1750 non-drone and 4000 drone samples as shown in the matrix).

As a further test, the standard deviation of the feature samples contained in the test vector for the classifier has been artificially increased by a factor ranging from 1.05 to 2.5 in steps. This was done to attempt to mimic the situation where additional new test data, on which the classifier has not been trained for, present a wider possible range of values around their original distribution. This could be due to different physical characteristics of the drones, their kinematic profile and trajectory, or even to lower SNR. The majority of our features are strongly correlated to the intensity patterns of the pixels in the micro-Doppler spectra, hence it is expected that reductions in SNR will worsen the separation of the feature samples for the different classes. Although these synthetic data

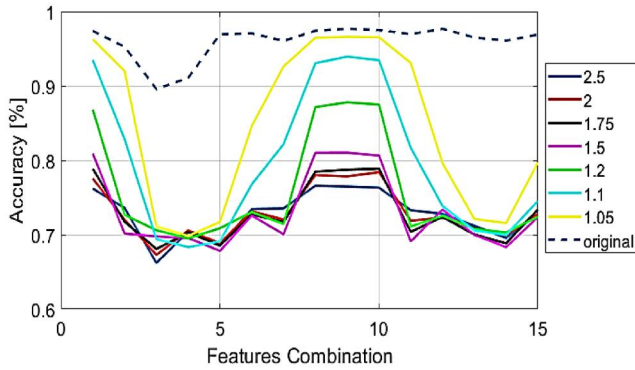


**FIGURE 12** Classification accuracy as a function of feature combinations for different increases of standard deviation in testing data samples. Ensemble (ET) classifier used in all cases; binary classification drone (L + X-band) versus non-drone data (L-band)

cannot substitute additional authentic experimental data which may contain true and different outliers, this test is useful to evaluate how the simple classification approach presented here responds to some changes in the test data.

Figure 12 shows the classification accuracy using the ET classifier for the different combinations of selected features, as in Figure 11, but with the different traces here referring to different scaling factors to increase the standard deviation. The dashed trace is the original result also shown in Figure 11, that is, with no scaling of the standard deviation. As expected, increased standard deviation in the test data corresponds to decreasing classification performance. This effect is however more evident for certain combinations of features rather than others, in a sign that some features may be to an extent more robust than others to variations in their values. Specifically, the single feature (previously denoted as feature A) used at combination #1 in Figure 12 (and also in Figure 11) appears to be more robust than the others to the changes in standard deviation. This is reinforced by the fact that combinations #8–10 in Figure 12 are all pairs of features containing feature A, namely AD; AC; AB. Note that this feature A was the maximum value of all pixels values in the negative region of the micro-Doppler spectrum.

### 3.3 | Discussion on the results

As mentioned in Section 3.2, it was not possible to acquire usable data of non-drone targets of opportunity at X-band. For this reason, a rigorous quantitative comparison of the performances at the two bands, L and X, is not possible with the initial data presented in this paper. However, it is possible to perform an analysis of the simple classification test for L-band only data, and then investigate the effect of mixing these data with some of the available X-band drone data. Figure 13 shows the results of this simple comparison using the ET classifier and the combinations of features described in Section 3.2. The three traces refer to:

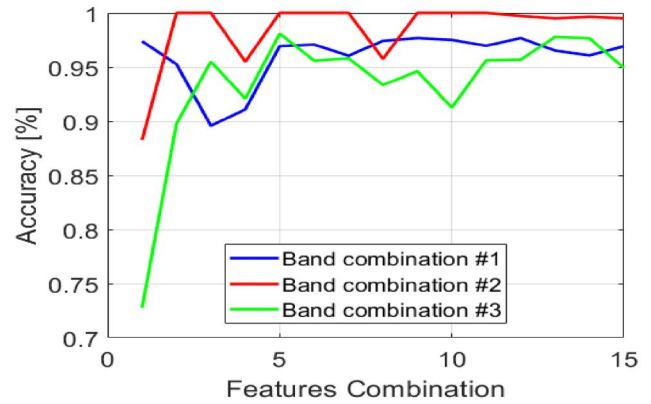


**FIGURE 13** Classification accuracy as a function of feature combinations for data at different bands: trace #1 X + L-band drone data; trace #2 L-band drone data only; trace #3 X-band drone data only. Non-drone data are always at L-band

1. Blue trace; binary classification drone (L + X-band data) versus non-drone data (L-band data)
2. Red trace; binary classification drone (L-band data only) versus non-drone data (L-band data)
3. Green trace; binary classification drone (X-band data only) versus non-drone data (L-band data only)

Trace one was already shown in Figure 11. Trace two shows that when using L-band data only, higher classification accuracy can be obtained, near 100% even using very few features. More interesting is to look at the performance for trace 3, where the classification algorithm is run in a multi-frequency manner, with the drone data collected at X-band and the non-drone data at L-band. The classification accuracy for the binary drone versus non-drone problem can reach above 95% with suitable feature combinations. While these numbers are computed over a small amount of data and feature samples, the results are encouraging to investigate further (a) the difference in scattering behaviour at the two frequency bands for drone and non-drone targets, and (b) the possible advantages in information fusion approaches that combine the two sources of data.

Another topic of discussion concerns the quantification of benefits of using a multistatic radar with respect to a conventional monostatic system. How better can certain radar performance metrics (e.g. classification accuracy, probability of detection, clutter properties) become when multiple bistatic nodes are used, and how many of such nodes are needed to achieve a noticeable benefit? To answer these excellent research questions through a rigorous quantitative analysis, one needs simultaneous recordings of the same targets and scene of interest.

Work performed with NetRAD, the predecessor of the radar presented in this article, allowed to partially answer these questions. For example, the work in [19–22] compared sea clutter properties relevant in radar detection processes for simultaneous monostatic and bistatic data at different bistatic angles (multistatic in case of [19]). These were, for example, the

amplitude statistics such as the shape parameter of the  $K + \text{Noise}$  distribution, spatial and temporal correlation, and average reflectivity. The analysis of these metrics showed significant ‘clutter diversity’, essentially different properties of the sea clutter recorded at monostatic and bistatic nodes, such as clutter presenting ‘less spiky’ statistics in some bistatic geometries. This can be exploited as new degrees of freedom in the design of radar systems in maritime applications [23].

The analysis in [3, 24] presented the classification of a drone (DJI Phantom) with/without small payloads attached to its body, comparing the performance in terms of classification accuracy when combining the multistatic data with different information fusion approaches (i.e. only monostatic data, feature fusion of multistatic data, and decision level fusion with different schemes). This provided a quantitative comparison of the gain in accuracy when multistatic, that is multi-perspective, information on the targets was used.

Further analysis was performed in [25] with corner reflectors in an indoor controlled scenario, and in [26, 27] in the context of outdoor surveillance for personnel identification and classification of unarmed versus potentially armed subjects. This work showed the advantage of using spatially diverse, multi-perspective information on the targets of interest and provided quantitative comparisons of monostatic and single-perspective data versus multistatic in terms of classification accuracy. Advantages of ‘feature diversity’ were also shown [27], that is how diversifying and adapting the classification scheme, namely the extracted features, at each radar node provided a performance gain compared to having all nodes working on the same features.

The aforementioned examples provide quantitative information on potential advantages of bistatic and multistatic radar, designing new radar capabilities in a diverse and flexible network rather than in a single stand-alone device [28]. The initial results in this article using the NeXtRAD system can provide some further insights for a quantitative monostatic versus bistatic comparison. For example, the results presented in Table 1 compare the SNR for simultaneous recordings of the same target by the monostatic node and one bistatic receiver, for small ( $\sim 9^\circ$ ) and large ( $\sim 90^\circ$ ) bistatic angles. While this comparison is still too ‘sparse’ as a function of  $\beta$  to draw robust conclusions, the results show the capabilities of the NeXtRAD system to address this question in a more systematic investigation in further work.

## 4 | CONCLUSIONS AND FUTURE WORK

This article has discussed examples of the capabilities of the multistatic multiband radar network, NeXtRAD, in measuring the radar signatures of small UAVs (mainly a DJI Matrice hexacopter) at large baselines (few kilometres), bistatic angles (of the order of  $90^\circ$ ) and bistatic ranges (few kilometres), at both X- and L-bands.

Empirical examples of range-time plots and micro-Doppler spectrograms have been presented, showing considerable SNR and a good level of details to characterise the

modulations of rotor blades and the signatures of birds of opportunity at distances in the order of several hundred metres. Based on these signatures, a simple classification scheme for binary drone versus non-drone discrimination has been developed. Ten empirically obtained features extracted from the micro-Doppler data and its SVD decomposition have been used, combined with feature selection and four supervised learning classifiers. The results show good performance, with accuracy above 90% up to a best average of 98% and minimum (worst case scenario across 50 cross-validation tests) of 95%.

While encouraging, these results were obtained with a relatively limited dataset due to the complexity of measuring targets from land to sea at relatively long distances. Nevertheless, the multistatic setup showed its capabilities and potential, and further analysis work is ongoing on the data collected, including those from a new experimental campaign performed in December 2019 and not showed in this article. This additional work include the investigation of a wider set of data with drones and birds targets, collected with different combinations of relevant parameters that can influence the classification results (e.g. polarisation, bistatic angles, SNR levels). More advanced spectral analysis tools, such as different time-frequency distributions and the wavelet transform, can be considered. Furthermore, the radar signatures can be matched with the data collected by the GPS logger mounted on the UAVs (latitude, longitude, measured speed, pitch and roll angles) and the images from the video cameras, in order to extract track-related information that could be exploited for implementing kinematic based classification schemes, without resorting to the use of micro-Doppler.

## ACKNOWLEDGEMENTS

The authors would like to thank A. Stevens, L. Clayton, B. Kahn, D. Du Plessis, J. Cilliers, S. Coetzee, S. Sandenbergh, T. Johnsen, and W. Miceli for the support provided during the measurement campaign, Masters student Y. Ding for data processing support, and the Office of Naval Research Global (USA), the Institution of Engineering and Technology, FFI Norway), and SA National Defence Force for funding this work.

## ORCID

Riccardo Palamà  <https://orcid.org/0000-0001-6121-9485>

Francesco Fioranelli  <https://orcid.org/0000-0001-8254-8093>

Matthew Ritchie  <https://orcid.org/0000-0001-8423-8064>

Michael Inggs  <https://orcid.org/0000-0003-2162-7710>

Hugh Griffiths  <https://orcid.org/0000-0002-9947-5553>

## REFERENCES

1. Patel, J.S., Fioranelli, F., Anderson, D.: Re-view of radar classification and RCS characterisation techniques for small UAVs or drones. *IET Radar, Sonar Navig.* 12(9), 911–919 (August 2018)
2. Rahman, S., Robertson, D.A.: Radar micro-Doppler signatures of drones and birds at K-band and W-band. *Nat. Scientific Rep.* 8, 17396 (2018)

3. Fioranelli, F., et al.: Classification of loaded/unloaded micro-drones using multistatic radar. *Electron. Lett.* 51(22), 1813–1815 (October 2015)
4. Ritchie, M., et al.: Monostatic and bistatic radar measurements of birds and micro-drone. *IEEE Radar Conference*, Philadelphia, PA (May 2016)
5. Hoffmann, F., et al.: Micro-Doppler based detection and tracking of UAVs with multistatic radar. *IEEE Radar Conference*, Philadelphia, PA (May 2016)
6. Derham, T.E., et al.: Design and evaluation of a low-cost multistatic netted radar system. *IET Radar, Sonar Navig.* 1, 362–368 (2007)
7. Palamà, R., et al.: Measurements of multistatic X&L band radar signatures of UAVs. *SEE International Radar Conference*, Toulon, France (September 2019)
8. Inggs, M., et al.: Multistatic radar: system requirements and experimental validation, pp. 1–6. *SEE International Radar Conference*, Lille (2014)
9. Alhuwaimel, S., et al.: First measurements with NeXtRAD, a polarimetric X/L band radar network. *IEEE Radar Conference (RadarConf)*, Seattle, WA, pp. 1663–1668 (2017)
10. Sandenbergh, J.: Synchronising coherent networked radar using low-cost GPS-disciplined oscillators, PhD thesis, University of Cape Town (2019). <https://open.uct.ac.za/handle/11427/30829>
11. Molchanov, P., et al.: Classification of small UAVs and birds by micro-Doppler signatures. *European Radar Conference*, Nuremberg (2013)
12. Jahangir, M., Baker, C.J.: Extended dwell Doppler characteristics of birds and micro-UAS at l-band, 2017 18th International Radar Symposium, Prague, pp. 1–10. (2017)
13. Torvik, B., Olsen, K.E., Griffiths, H.: Classification of birds and UAVs based on radar polarimetry. *IEEE Geosci. Remote Sensing Lett.* 13(9), 1305–1309 (September 2016)
14. Rahman, S., Robertson, D.A.: Classification of drones and birds using convolutional neural networks applied to radar micro-Doppler spectrogram images. *IET Radar, Sonar Navig.* 14(5), 653–661 (2020)
15. Huizing, A., et al.: Deep learning for classification of mini-UAVs using micro-Doppler spectrograms in cognitive radar. *IEEE Aero. Electron. Syst. Mag.* 34(11) (2019)
16. Cai, Y., Krasnov, O., Yarovoy, A.: Radar recognition of multi-propeller drones using micro-Doppler linear spectra, 16th European Radar Conference (EuRAD), France, Paris (October 2019)
17. Gürbüz, S.Z., et al.: Operational assessment and adaptive selection of micro-Doppler features. *IET Radar, Sonar Navig.* 9(9), 1196–1204 (12 2015)
18. Breiman, L.: Bagging predictors. *Mach. Learn.* 24, 123–140 (1996)
19. Fioranelli, F., et al.: Analysis of polarimetric bistatic sea clutter using the NetRAD radar system *IET Radar, Sonar Navig.* 8, vol. 10, pp. 1356–1366 (2016)
20. Palamà, R., et al.: Correlation analysis of simultaneously collected bistatic and monostatic sea clutter, 2017 *IEEE Radar Conference (RadarConf)*, Seattle, WA, pp. 1466–1471 (2017)
21. Al-Ashwal, W.A., Woodbridge, K., Griffiths, H.D.: Analysis of bistatic sea clutter – Part I: average reflectivity. *IEEE Trans. Aerosp. Electron. Syst.* 50(2), 1283–1292 (April 2014)
22. Al-Ashwal, W.A., Woodbridge, K., Griffiths, H.D.: Analysis of bistatic sea clutter – Part II: amplitude statistics. *IEEE Trans. Aerosp. Electron. Syst.* 50(2), 1293–1303 (April 2014)
23. Klemm, R., et al. (eds.): *Novel Radar Techniques and Applications*, vol. 2, Chapter 6: Clutter diversity, Scitech Publishing (2018)
24. Ritchie, M., et al.: Multistatic micro-Doppler radar feature extraction for classification of unloaded/loaded micro-drones. *IET Radar, Sonar Navig.* vol. 11, pp. 116–124 (2017)
25. Vespe, M., Baker, C.J., Griffiths, H.D.: Radar target classification using multiple perspectives *IET Radar, Sonar Navig.*, vol. 1, pp. 300–307 (August 2007)
26. Fioranelli, F., Ritchie, M., Griffiths, H.: Performance analysis of centroid and SVD features for personnel recognition using multistatic micro-Doppler. *IEEE Geosci. Remote Sensing Lett.* 13(5), 725–729 (May 2016)
27. Fioranelli, F., et al.: Feature diversity for optimised human micro-Doppler classification using multistatic radar. *IEEE Trans. Aerosp. Electron. Syst.* 53(2), 640–654 (April 2017)
28. *Novel Radar Techniques and Applications*, (eds.). In: Chapter 8: The concept of the intelligent radar network, Vol. 2, Chapter 8: Scitech Publishing (2018)

**How to cite this article:** Palamà R, Fioranelli F, Ritchie M, Inggs M, Lewis S, Griffiths H. Measurements and discrimination of drones and birds with a multi-frequency multistatic radar system. *IET Radar Sonar Navig.* 2021;1–12. <https://doi.org/10.1049/rsn2.12060>